Coastal Engineering 176 (2022) 104167

Contents lists available at ScienceDirect

Coastal Engineering

journal homepage: www.elsevier.com/locate/coastaleng

Reconstruction of nearshore wave fields based on physics-informed neural networks

Nan Wang [a], Qin Chen [b,*], Zhao Chen [c]

[a] Department of Civil and Environmental Engineering, Northeastern University, 400 SN, MA, 02115, Boston, United States
[b] Department of Civil and Environmental Engineering, Northeastern University, 471 SN, MA, 02115, Boston, United States
[c] Department of Civil and Environmental Engineering, Northeastern University, 360 Huntington avenue, MA, 02115, Boston, United States

ARTICLE INFO

Keywords:
Physics-informed neural networks
Wave field reconstruction
Numerical modeling
Nearshore wave processes

ABSTRACT

This paper focuses on utilizing physics-informed neural networks (PINNs) to model nearshore wave transformation. The nearshore wave nets (*NWnets*), which integrate the prior knowledge of wave mechanics (i.e., the wave energy balance equation and dispersion relation) and fully connected neural networks, are developed to reconstruct nearshore wave fields with scarce wave measurements. The performance of the *NWnets* is examined by comparing the PINN outputs with numerical solutions from XBeach and experimental data over a two-dimensional alongshore uniform barred beach and a three-dimensional circular shoal, respectively. It is found that the test errors are reasonably small with wave height measurements at only three locations applied as the training data for the alongshore uniform barred beach. Moreover, the *NWnets* are able to reconstruct the entire wave field and capture the focusing and defocusing of wave energy with sufficient accuracy over the circular shoal when a small amount of wave height measurements from the laboratory experiment are employed as the training data. The influence of network sizes, collocation points, training points, and the resolution of wave directional spreading on the performance of the *NWnets* is investigated. The adaptive learning rate annealing algorithm is utilized to calculate weighting coefficients for balancing the interplay between different loss terms in the total loss functions. Several illustrative examples of transfer learning are also provided, which can accelerate the training of *NWnets* for modeling waves under different boundary and bathymetric conditions. Our results show that the physics-guided deep learning method is a promising tool for studying nearshore processes.

1. Introduction

Wave information is required for designing and operating many coastal projects. However, in-situ wave measurements are often spatiotemporally sparse because of high costs (Malekmohamadi et al., 2011). Thus, nearshore wave information is usually simulated indirectly from wind fields using physics-based numerical models (e.g., Booij et al., 1999; Tolman, 1991) and soft computing-based models (e.g., James et al., 2018; Wei and Davison, 2022).

Significant progress has been made in physics-based numerical modeling based on wave action and momentum balance principles during the last several decades. For instance, the WAve Model (WAM, Hasselmann et al., 1988; Brown, 2010; Hasselmann et al., 1988) and the WAVEWATCH model (Tolman, 1991; Mentaschi et al., 2015) can be used to simulate ocean waves. Phase-averaged spectral models such as XBeach (Roelvink et al., 2009) and Simulating WAves Nearshore (SWAN, Booij et al., 1999) can be utilized to predict wave propagation over domains extending thousands of meters from the shoreline. For projects with a limited size of hundreds of meters in nearshore regions, phase-resolving models based on Boussinesq-type equations or Euler equations for fluid motions can be applied (e.g., Chen et al., 2000; Shi et al., 2012; Lynett et al., 2002; Ma et al., 2012; Zijlema et al., 2011; Sørensen et al., 2004; Salatin et al., 2021). However, these physics-based models require a precise description of initial and boundary conditions to simulate the wave and flow fields accurately (Kissas et al., 2020). Since it can be challenging to resolve real-world physical problems with noisy or missing wave boundary conditions (i.e., ill-posed problems) through conventional numerical models (e.g., Karniadakis et al., 2021), nested computational domains may be required to provide boundary conditions, which are usually time-consuming to apply and prone to errors. Additionally, traditional wave models involve the cumbersome generation of computational meshes for complicated geometries. As an

* Corresponding author.
E-mail addresses: wang.nan@northeastern.edu (N. Wang), q.chen@northeastern.edu (Q. Chen), chen.zhao1@northeastern.edu (Z. Chen).

https://doi.org/10.1016/j.coastaleng.2022.104167
Received 29 April 2022; Received in revised form 16 June 2022; Accepted 23 June 2022
Available online 27 June 2022

alternative, soft computing-based models could be used as surrogates to reduce the computational burden as they can handle strong nonlinearity and high dimensionality (e.g., Sun et al., 2020).

Many data-driven models have been developed to study nonlinear relationships between input features and labels for coastal engineering applications during the last two decades, such as artificial neural networks (ANN), Bayesian networks (BN), support vector machines (SVM), decision trees, and fuzzy inference systems (FIS) (e.g., Deo and Naidu, 1998; Deo et al., 2001; Jain et al., 2011; Peres et al., 2015; Cornejo-Bueno et al., 2016; Sadeghifar et al., 2017; Parker and Hill 2017; Oh and Suh, 2018; Stringari et al., 2019; Zheng et al., 2020; Chen et al., 2021; Wei, 2021; Miky et al., 2021; Jörges et al., 2021; Elbisy and Elbisy, 2021; Bento et al., 2021; Mares-Nasarre et al., 2021; Lee et al., 2021; Wang et al., 2022a; Wang et al., 2022b). For instance, Malekmohamadi et al. (2011) compared the performance of ANN, BN, SVM, and Adaptive Neuro FIS methods for estimating wave height with wind data in Lake Superior, USA. Their results show that all these methods could provide acceptable predictions for H_s, except for BN. ANNs and SVMs were applied by James et al. (2018) to surrogate SWAN for simulating significant wave height (H_s) and characteristic wave period, respectively. Their model exhibited a similar level of accuracy for wave prediction and ran over 4000 times faster than SWAN. However, the direct application of these soft-computing models to scientific domains has some challenges. For instance, data availability is often limited in reality, while a huge amount of training data is required in traditional machine learning (ML) models. Additionally, traditional ML models cannot be generalized to predict scenarios that are unseen in the training dataset. Most importantly, traditional ML models may produce results inconsistent with physical laws because those models do not consider any physics (e.g., Karpatne et al., 2017; Jia et al., 2019).

A considerable amount of prior knowledge can be utilized in ML practice for cases related to the modeling of physical systems. To combine scientific knowledge and data, the research community is beginning to integrate physics with soft-computing learning algorithms (e.g., Zhang et al., 2019; Willard et al., 2020; Chen et al., 2021; Chen and Sun, 2021; Chen et al., 2022). For instance, Raissi et al. (2019) used the physics-informed neural networks (PINNs) to solve multi-dimensional partial differential equations. Given potentially noisy and scattered data on velocity components, they managed to identify the unknown parameters in Navier-Stokes equations and obtain an accurate reconstruction of the pressure field in the cylinder wake. Jia et al. (2019) developed the PGRNN (physics-guided recurrent neural network) model to capture lake temperature dynamics by integrating energy conservation and a density-depth constraint into recurrent neural networks. They found that PGRNN can achieve good generalizability and improve prediction accuracy over that of physics-based numerical models. Moreover, Jin et al. (2021) proposed the Navier-Stokes flow nets (*NSFnets*) to reconstruct incompressible turbulent and laminar flows. They overcame the ill-posed inverse problems in solving the Navier-Stokes equations by integrating the governing equations and deep neural networks through automatic differentiation.

In general, the results from these studies indicate that PINNs can be effectively applied to solve forward and inverse problems that are ill-posed (Karniadakis et al., 2021). Compared with conventional ML models, the advantages of PINNs can be mainly attributed to the fact that encoding prior knowledge during the training process can constrain learning and compensate for the insufficiency of the data. Thus, such models can remain robust even with inaccurate or missing input data and give accurate predictions consistent with physical laws (Willard et al., 2020; Wang et al., 2020; Chen et al., 2021). It is worth mentioning that the mathematical data assimilation method can also be used to solve ill-posed inverse problems by minimizing the difference between model predictions and observations (e.g., Salim and Wilson, 2021). For instance, data assimilation methods have been utilized to identify unknown model parameters by Wilson et al. (2010), Kurapov et al. (2007), and Wilson and Berezhnoy (2018), among others. Even though data assimilation methods have been developed for decades, the spatiotemporal heterogeneity of available datasets calls for new transformative models (Karniadakis et al., 2021). Therefore, this work is aimed at generating a novel framework with PINNs for reconstructing wave fields by combining the underlying governing equations with available data. Unlike the data assimilation method, our proposed method does not require simulations from a deterministic forward numerical model or knowledge about the uncertainty of observations and the uncertainty of the numerical model.

In this study, a composite PINN model, *NWnets* (nearshore wave nets), was developed to reconstruct wave fields in the nearshore with scarce wave measurements. Wave shoaling, refraction, and depth-limited breaking were considered in the *NWnets*. The governing equations encoded into the fully connected neural networks contain the wave energy balance equation and dispersion relation. The simulation accuracy of the *NWnets* was investigated on a two-dimensional alongshore uniform barred beach and a three-dimensional circular shoal, where the wave data were obtained from the XBeach simulation and laboratory experiments, respectively. To the best of our knowledge, the proposed *NWnets* are the first PINN model integrating the wave energy balance equation and dispersion relation with limited experimental data to reconstruct nearshore wave fields. The rest of the paper is organized as follows. Section 2 introduces the governing equations and the laboratory experiment of wave propagation over a circular shoal. The details of the model setup for PINNs and XBeach are introduced in this section. Section 3 examines the performance of PINNs in reconstructing nearshore wave fields by comparing the outputs with the XBeach-simulated and experimental data. Section 4 discusses the influences of network structures, the number of collocation points, the location of training data, and the resolution of directional spreading on the performance of the *NWnets*. Finally, Section 5 concludes the paper with remarks on this study.

2. Methodology

2.1. Energy balance equation for wave propagation in nearshore areas

Models for simulating waves without the influence of currents are generally based on the energy balance equation. The wave energy density can be regarded as a slowly varying function in space (x, y) and time t. In this study, we focused on stationary wave fields without wind forcing and ambient currents to examine the performance of the *NWnets*. Similar to the numerical model for hindcasting shallow water waves (HISWA), the directional distribution of the energy density was included in the model, but the frequency spectrum was represented by a frequency (Holthuijsen et al., 1989). In this study, we only considered wave shoaling, refraction, and depth-limited wave breaking. Thus, the wave energy balance equation is given by

$$\frac{\partial ec_{gx}}{\partial x} + \frac{\partial ec_{gy}}{\partial y} + \frac{\partial ec_{g\theta}}{\partial \theta} + d_w = 0 \tag{1}$$

where e is the wave energy density in each directional bin, θ represents the angle of incidence with respect to the x-axis, and d_w is the dissipation of energy density caused by wave breaking. The wave propagation speeds in x, y, and directional space are formulated as

$$c_{gx}(x, y, \theta) = c_g \cos\theta \tag{2}$$

$$c_{gy}(x, y, \theta) = c_g \sin\theta \tag{3}$$

$$c_\theta\ (x, y, \theta) = \frac{\omega}{\sinh 2kh}\left(\frac{\partial h}{\partial x}\sin\theta - \frac{\partial h}{\partial y}\cos\theta\right) \tag{4}$$

where h represents the local water depth, k is the wave number, c_g is the group velocity, and ω is the angular frequency. The dispersion relation relates the wave number of a wave to its frequency as

$$\omega^2 - gk\tanh(kh) = 0 \tag{5}$$

The total wave energy E and the mean wave direction are given by

$$E = \int_0^{2\pi} e(\theta)d\theta \tag{6}$$

and

$$\theta_{\mathrm{m}} = \frac{1}{E}\int_0^{2\pi} \theta e(\theta)d\theta \tag{7}$$

The Janssen and Battjes (2007) formulation for wave breaking was applied in this study as

$$\overline{D}_w = \frac{3\sqrt{\pi}\alpha f\rho g H_{\mathrm{rms}}^3}{16h}Q_b \tag{8}$$

$$Q_b = 1 + \frac{4}{3\sqrt{\pi}}\left(R^3 + \frac{3}{2}R\right)\exp\left(-R^2\right) - erf(R) \tag{9}$$

$$R = \frac{H_b}{H_{\mathrm{rms}}} \tag{10}$$

$$H_b = \frac{0.88}{k}\tanh\left[\frac{\gamma kh}{0.88}\right] \tag{11}$$

where $\overline{D}_w$ denotes the expected value of the power dissipated per unit area, Q_b is the fraction of breaking waves, H_b represents the breaking wave height, γ is the wave breaking parameter, H_{rms} is the root-mean-square wave height, and f is the frequency. $\alpha = 1$ was applied in this study as the wave dissipation coefficient. ρ and g are the water density and gravitational acceleration, respectively. The total wave dissipation was distributed proportionally over the wave directions using the following formulation

$$d_w(x,y,\theta) = \frac{e(x,y,\theta)}{E(x,y)}\overline{D}_w(x,y) \tag{12}$$

The root-mean-square wave height was calculated based on

$$H_{\mathrm{rms}} = \sqrt{\frac{8E}{\rho g}} \tag{13}$$

2.2. Physics-informed neural networks

PINN model is a recently proposed deep learning method, which infuses the governing equations into the artificial neural networks and enriches the loss function by adding residual terms based on the physical laws or equations. It bridges the gap between ML-based methods and scientific computations to deduce parameters, solutions, and physical laws involving partial differential equations (Kissas et al., 2020). In this study, a novel composite PINN model was developed to find the solutions of Eqn (1) and Eqn (5) for reconstructing wave fields in the nearshore. The corresponding residuals were defined as

$$f_1(x,y,\theta) := \frac{\partial ec_{gx}}{\partial x} + \frac{\partial ec_{gy}}{\partial y} + \frac{\partial ec_{g\theta}}{\partial \theta} + d_w \tag{14}$$

$$f_2(x,y) := \omega^2 - gk\tanh(kh) \tag{15}$$

These residuals were applied as restraints during the training of the *NWnets* to generate physically consistent predictions. Moreover, the *NWnets* were also constrained to fit the available measurements (e.g., H_{rms} and θ_{m}) scattered in the computational domain. Since the wave energy density depends on (x,y,θ) while wave numbers are only related to (x,y), composite neural networks were utilized to model nearshore wave propagation in this study. The schematic representation of the *NWnets* algorithm is shown in Fig. 1.

It is seen in Fig. 1 that the loss function for the *NWnets* consists of two parts. The first part corresponds to the collocation points (i.e., residual loss), where the physical constraints were imposed to encourage Eqns (14) and (15) to equal zero. In general, the collocation points could be grid points or random points inside the computational domain (Lu et al., 2021), and the former one was applied in this study. The partial derivatives in the residual expression were computed by automatic differentiation (e.g., Kissas et al., 2020). The second part encouraged the outputs of *NWnets* to match H_{rms}, θ_{m}, and h obtained from field observations (using the XBeach simulations in this study for PINN testing) or laboratory experiments (i.e., measurement loss). Therefore, the total loss function for the *NWnets* is given as

$$\mathscr{L}_{total} = \mathscr{L}_{residual} + \mathscr{L}_{measurements} = \mathscr{L}_{f_1} + \lambda_{f_2}\times\mathscr{L}_{f_2} + \lambda_{H_{\mathrm{rms}}}\times\mathscr{L}_{H_{\mathrm{rms}}} + \lambda_{\theta_{\mathrm{m}}}\times\mathscr{L}_{\theta_{\mathrm{m}}} + \lambda_h\times\mathscr{L}_h \tag{16}$$

where λ_{f_2}, $\lambda_{H_{\mathrm{rms}}}$, $\lambda_{\theta_{\mathrm{m}}}$, and λ_h are the weighting coefficients for balancing the interplay between different terms in the loss function. It is worth emphasizing that only the measurement loss is used in the traditional ANN models to reduce modeling errors. In the *NWnets*, the mean squared error (*MSE*) was employed to represent the loss functions and is given for each term by

$$\mathscr{L}_{f_1} = \frac{1}{N_f}\sum_{i=1}^{N_f}\left(f_1^i\left(x_f^i, y_f^i, \theta_f^i\right)\right)^2 \tag{17}$$

$$\mathscr{L}_{f_2} = \frac{1}{N_f}\sum_{i=1}^{N_f}\left(f_2^i\left(x_f^i, y_f^i\right)\right)^2 \tag{18}$$

$$\mathscr{L}_{H_{\mathrm{rms}}} = \frac{1}{N_{H_{\mathrm{rms}}}}\sum_{i=1}^{N_{H_{\mathrm{rms}}}}\left({H_{\mathrm{rms}}}^i\left(x_{H_{\mathrm{rms}}}^i, y_{H_{\mathrm{rms}}}^i\right) - {H_{\mathrm{rms}}^*}^i\right)^2 \tag{19}$$

$$\mathscr{L}_{\theta_{\mathrm{m}}} = \frac{1}{N_{\theta_{\mathrm{m}}}}\sum_{i=1}^{N_{\theta_{\mathrm{m}}}}\left({\theta_{\mathrm{m}}}^i\left(x_{\theta_m}^i, y_{\theta_m}^i\right) - {\theta_{\mathrm{m}}^*}^i\right)^2 \tag{20}$$

$$\mathscr{L}_h = \frac{1}{N_h}\sum_{i=1}^{N_h}\left(h^i\left(x_h^i, y_h^i\right) - {h^*}^i\right)^2 \tag{21}$$

where $\{{H_{\mathrm{rms}}}^i(x_{H_{\mathrm{rms}}}^i, y_{H_{\mathrm{rms}}}^i)\}_{i=1}^{N_{H\mathrm{rms}}}$, $\{{\theta_{\mathrm{m}}}^i(x_{\theta_m}^i, y_{\theta_m}^i)\}_{i=1}^{N_{\theta\mathrm{m}}}$, and $\{h^i(x_h^i, y_h^i)\}_{i=1}^{N_h}$ denote the PINN outputs of H_{rms}, θ_{m}, and h, respectively. H_{rms}^*, θ_{m}^*, and h^* are the targets (labels) of H_{rms}, θ_{m}, and h, respectively. $\{(x_f^i, y_f^i, \theta_f^i)\}_{i=1}^{N_{H\mathrm{rms}}}$ represents collocation points that are uniformly placed inside the computational domain for minimizing the loss of residuals.

In this study, two test scenarios were employed to assess the performance of *NWnets* for solving the energy balance equation and dispersion relation, including reconstructing wave fields over a two-dimensional alongshore uniform barred beach and a three-dimensional circular shoal. We applied relatively simple feedforward neural networks throughout this study without additional regularization (e.g., dropout or L1/L2 penalties). Hyperbolic tangent was used as the activation function. All the networks were initialized with Xavier initialization (Glorot and Bengio, 2010). Normalization was carried out to keep the input and output between −1 and 1, and the corresponding governing equations were also normalized by the same factors (Jin et al., 2021). As a result, network weights and biases could have values of similar magnitudes, and the negative impact of the large difference between various parameters could be avoided. The network structure of *NWnets* was kept identical to four hidden layers of 30 nodes for each test case. A discussion about the influence of network structures on the performance of *NWnets* is presented in Section 4.2.1. More details on the selected optimizer, learning rates, and settings of the measurements and

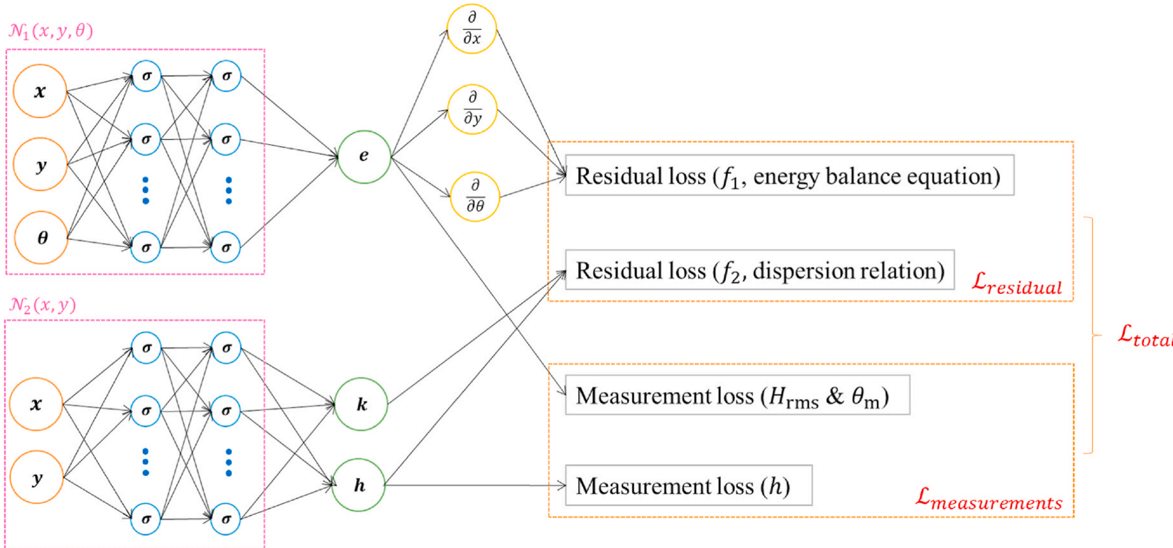

Fig. 1. A schematic representation of the proposed algorithm for the *NWnets*.

collocation points for the two test scenarios shall be given in Section 2.2.1 and 2.2.2. In this study, the training was implemented on an NVIDA v100-sxm2 GPU with the TensorFlow platform.

2.2.1. *Alongshore uniform barred beach*

The wave condition offshore of the alongshore uniform barred beach was set as $H_{\mathrm{rms}} = 1$ m and peak wave period (T_{p}) $= 8$ s. The peak wave period remains constant over the entire computational domain. The incident wave angle follows the directional distribution of $\cos^{\mathrm{m}}(\theta - \theta_{\mathrm{m}})$ with $\theta_{\mathrm{m}} = -30^{\circ}$ and m $= 8$, 20, 32, and 130. Fig. 2 shows the bathymetry of the alongshore uniform barred beach. The cross-shore distance from the offshore location was set as x, and the entire computational domain extended from $x = 0$ to 1000 m. Since the study area is uniform in the longshore direction, the input features to the *NWnets* only included x and θ. It was assumed that the water depth was known at every location, meaning that the water depth data over the entire study area were used as training data for the model. The training data for H_{rms} and θ_{m} were set at the locations listed in Table 1. A total of 1000 collocation points were uniformly distributed from $x = 0$ to 1000 m to constrain learning for generating physically consistent predictions.

Numerical simulations of H_{rms} and θ_{m} from XBeach were employed as training and testing data for developing the *NWnets* to reconstruct waves over the alongshore uniform barred beach. The resolution of directional spreading of waves ($d\theta$) was set to 1° in both XBeach and PINN models, and the lower and upper directional limits were defined as −90° and 90°, respectively. Adam (adaptive moment estimation) and L-BFGS-B (limited memory Broyden–Fletcher–Goldfarb–Shanno with boundaries) were used as network training functions (e.g., Kingma and Ba, 2014; Liu and Nocedal, 1989). The Adam optimizer was employed to produce a better set of initial neural network variables, and L-BFGS-B was used to further fine-tune the PINN networks for minimizing test errors (Jin et al., 2021). The initial learning rate of Adam was set to 10^{-4} and then decreased to 80% of the previous rate every 5000 iterations. 4×10^4 Adam iterations were implemented before the L-BFGS-B training, which was then automatically terminated based on the increment tolerance. More discussions on the influences of locations of training points, collocation points, and the resolution of directional spreading on the performance of *NWnets* are presented in Section 4.2.

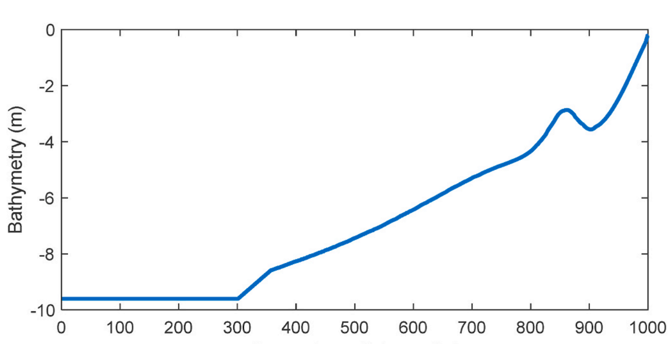

Fig. 2. The cross-shore profile of the alongshore uniform barred beach.

Table 1
The locations of training points of H_{rms} and θ_m for reconstructing wave fields over the alongshore uniform barred beach.

	Locations of training points
H_{rms}	x $= 100, 500, 900$ m
θ_{m}	x $= 500$ m

2.2.2. *Circular shoal*

A series of laboratory experiments on wave propagation over a circular shoal were carried out by Chawla et al. (1996) in a directional wave basin. Several wave models have used this dataset as the testbed, such as the spectral wave model based on the mild-slope equation (Chawla et al., 1998), the time-domain Boussinesq model (Chen et al., 2000), and the curvilinear spectral wave model (Chen et al., 2005). In this study, test case 4 of the laboratory experiments with the directional random wave input was utilized as the testbed to examine the performance of *NWnets*.

The plan view of the wave basin and the transects of wave gauge locations are shown in Fig. 3. The wave basin was 18 m long and 18.2 m wide. The center of the shoal was located at $x = 5$ m and $y = 8.98$ m. The perimeter of the shoal is calculated with

$$(x-5)^2 + (y-8.98)^2 = (2.57)^2 \tag{22}$$

and the water depth is given by

$$h = h_o + 8.73 - \sqrt{82.81 - (x-5)^2 - (y-8.98)^2} \tag{23}$$

where h_o is the water depth of the flat bottom. In test case 4, the flat bottom of the basin has a water depth of 0.4 m, leading to a minimum

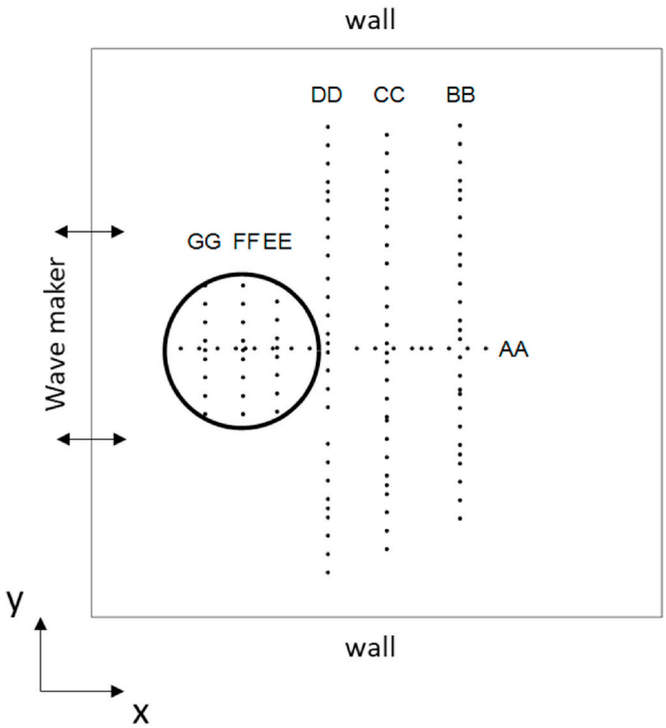

Fig. 3. Schematic view of the experimental setup and transects of wave gauge locations (Chawla et al., 1996). The black dots represent the 126 locations of wave height measurements.

water depth of 3 cm on the top of the circular shoal. The incident waves at the offshore boundary have $H_{\text{rms}} = 1.103$ cm and $T_p = 0.73$ s. The angular standard deviation of the directional spreading function is 20°. During the laboratory experiments, a total of 126 measurement points were set to record the wave heights in test case 4 (Fig. 3).

For reconstructing the wave field over the circular shoal, a PINN model was developed with input features including x, y, and θ. The training data for the model included the measurements of H_{rms} (or $E = \frac{1}{8}\rho g H_{\text{rms}}^2$) and h. Because wave directions were not measured in the laboratory experiment, they were not employed as training data for developing the *NWnets* to reconstruct the wave field over the circular shoal. To examine the influence of training points on the performance of the *NWnets*, we used 50%, 25%, 16.7%, and 12.5% of the 126 H_{rms} measurements as training data to reconstruct the entire wave field, leading to 63, 31, 21, and 15 training points of H_{rms} for each case, respectively. Based on Chawla et al. (1996), substantial spatial variations of the wave field over the circular shoal were observed (Fig. 5). Specifically, wave energy focuses on the top of the shoal due to depth-induced refraction. Wave breaking occurred over the circular shoal (Chen et al., 2005). In the leeside of the shoal, the wave height was smaller due to the defocusing of wave energy. Also, wave diffraction and wave interference occurred over the domain (Smit et al., 2015). To ensure the *NWnets* capture the wave height variation over the entire computational domain, the training points of H_{rms} were randomly placed along the seven transects (Fig. 3). Ten validation points of H_{rms} were selected randomly from the rest of the dataset, and the remaining data were utilized as testing points. Similarly, it was assumed that the water depth was known at every location, and the wave period was constant over the entire computational domain.

The computational domain extends from $x = 0$ to $x = 15$ m and from $y = 0$ to $y = 18$ m with a resolution of 0.2 m. The corresponding water depth data at each computational grid ($91 \times 76 = 6916$ points) were calculated using Eqn (23). As mentioned above, the collocation points could be grid points or random points inside the computational domain. However, if a vast number of collocation points were defined, it would be computationally expensive to evaluate the loss and gradient in each iteration in this study (e.g., Lu et al., 2021), because the model has three input features (i.e., x, y and θ) for simulating wave propagation over the circular shoal. By balancing the computational cost with the simulation accuracy, the collocation points were set at each computational grid, leading to 6916 collocation points. The resolution of directional spreading of waves was set to 10° in the *NWnets,* and the lower and upper directional limits were defined as −90° and 90°, respectively.

Similar to the *NWnets* for reconstructing wave fields over the alongshore uniform barred beach, Adam and L-BFGS-B were used as network training functions, with 8×10^4 Adam iterations conducted before L-BFGS-B started. To examine the prediction performance of the *NWnets*, the outputs of H_{rms} were compared to the experimental data from Chawla et al. (1996). Since the wave angle was not employed as training data for reconstructing the wave field over the circular shoal, the term related to the mean wave angle was removed from the total loss function during the training (i.e., $\lambda_{\theta_m} \times \mathscr{L}_{\theta_m}$ was removed from Eqn (16)). If the wave angle measurements are available in other test scenarios, we will apply the wave angle measurements as one of the training data to improve the performance of the *NWnets*.

2.3. Adaptive learning rate annealing algorithm

In Eqn (16), the weighting coefficients λ_{f_2}, $\lambda_{H_{\text{rms}}}$, λ_{θ_m}, and λ_h were employed for balancing the interplay between different terms in the loss function and increasing the rate of convergence during the training process. However, it is time-consuming to tune these weights by trial and error. Moreover, the optimal values for different weights are problem-dependent, so it is tedious to tune weights manually for different test scenarios (Jin et al., 2021). Thus, this study used the learning rate annealing algorithm to balance different terms in composite loss functions during the Adam training. The algorithm can improve the simulation accuracy by applying gradient statistics to determine proper weights adaptively to each term in loss functions (e.g., Wang et al., 2020). In this study, the weighting coefficients during L-BFGS-B were kept the same as the last ones applied in the Adam training.

In general, the parameters Θ of the *NWnets* can be formulated as

$$\Theta^{(n+1)} = \Theta^{(n)} - \eta \nabla_\Theta \mathscr{L}_{f_1} - \eta \lambda_{f_2} \nabla_\Theta \mathscr{L}_{f_2} - \eta \lambda_{H_{\text{rms}}} \nabla_\Theta \mathscr{L}_{H_{\text{rms}}} - \eta \lambda_{\theta_m} \nabla_\Theta \mathscr{L}_{\theta_m} - \eta \lambda_h \nabla_\Theta \mathscr{L}_h \tag{24}$$

where Θ represents the weights of all fully connected layers, η denotes the learning rate, and n is the iteration step. When the adaptive learning rate annealing algorithm is applied, the estimates of λ_{f_2}, $\lambda_{H_{\text{rms}}}$, λ_{θ_m}, and λ_h at each training step can be expressed by

$$\hat{\lambda}_{f_2}^{(n+1)} = \frac{max_\Theta(|\nabla_\Theta \mathscr{L}_{f_1}|)}{\overline{|\nabla_\Theta \lambda_{f_2}^{(n)} \mathscr{L}_{f_2}|}} \tag{25}$$

$$\hat{\lambda}_{H_{\text{rms}}}^{(n+1)} = \frac{max_\Theta(|\nabla_\Theta \mathscr{L}_{f_1}|)}{\overline{|\nabla_\Theta \lambda_{H_{\text{rms}}}^{(n)} \mathscr{L}_{fH_{\text{rms}}}|}} \tag{26}$$

$$\hat{\lambda}_{\theta_m}^{(n+1)} = \frac{max_\Theta(|\nabla_\Theta \mathscr{L}_{f_1}|)}{\overline{|\nabla_\Theta \lambda_{\theta_m}^{(n)} \mathscr{L}_{f\theta_m}|}} \tag{27}$$

$$\hat{\lambda}_h^{(n+1)} = \frac{max_\Theta(|\nabla_\Theta \mathscr{L}_{f_1}|)}{\overline{|\nabla_\Theta \lambda_h^{(n)} \mathscr{L}_{f_h}|}} \tag{28}$$

Then, λ_{f_2}, $\lambda_{H_{\text{rms}}}$, λ_{θ_m}, and λ_h for the next iteration are updated with the moving average method as

$$\lambda_{f_2}^{(n+1)} = (1-\beta)\lambda_{f_2}^{(n)} + \beta\widehat{\lambda}_{f_2}^{(n+1)} \tag{29}$$

$$\lambda_{H_{\mathrm{rms}}}^{(n+1)} = (1-\beta)\lambda_{H_{\mathrm{rms}}}^{(n)} + \beta\widehat{\lambda}_{H_{\mathrm{rms}}}^{(n+1)} \tag{30}$$

$$\lambda_{\theta_{\mathrm{m}}}^{(n+1)} = (1-\beta)\lambda_{\theta_{\mathrm{m}}}^{(n)} + \beta\widehat{\lambda}_{\theta_{\mathrm{m}}}^{(n+1)} \tag{31}$$

$$\lambda_{h}^{(n+1)} = (1-\beta)\lambda_{h}^{(n)} + \beta\widehat{\lambda}_{h}^{(n+1)} \tag{32}$$

where β is a hyperparameter representing how fast the contribution of previous weighting coefficients decreases (Wang et al., 2020). In this study, β was set to 0.1 to ensure the adaptation to be stable during the training process. The initial values for λ_{f_2}, $\lambda_{H_{\mathrm{rms}}}$, λ_{θ_m}, and λ_h were all set to 1.

2.4. Physics-based wave model (XBeach)

XBeach is a two-dimensional numerical model for simulating near-shore processes such as wave breaking, dune erosion, overwashing, and breaching (Roelvink et al., 2009). The model solves the short wave action balance equation given by

$$\frac{\partial N}{\partial t} + \frac{\partial (c_{gx}N)}{\partial x} + \frac{\partial (c_{gy}N)}{\partial y} + \frac{\partial (c_{g\theta}N)}{\partial \theta} = \frac{S}{\sigma} \tag{33}$$

where N is the wave action density, (x, y) are the horizontal Cartesian coordinates, t is the time, θ is the wave direction taken counterclockwise from the geographical east, and σ is the intrinsic radian frequency. c_{gx}, c_{gy}, and $c_{g\theta}$ represent wave energy propagation speeds in x, y, and directional spaces, respectively. On the right-hand side, S denotes the source terms of energy dissipation caused by wave breaking, bottom

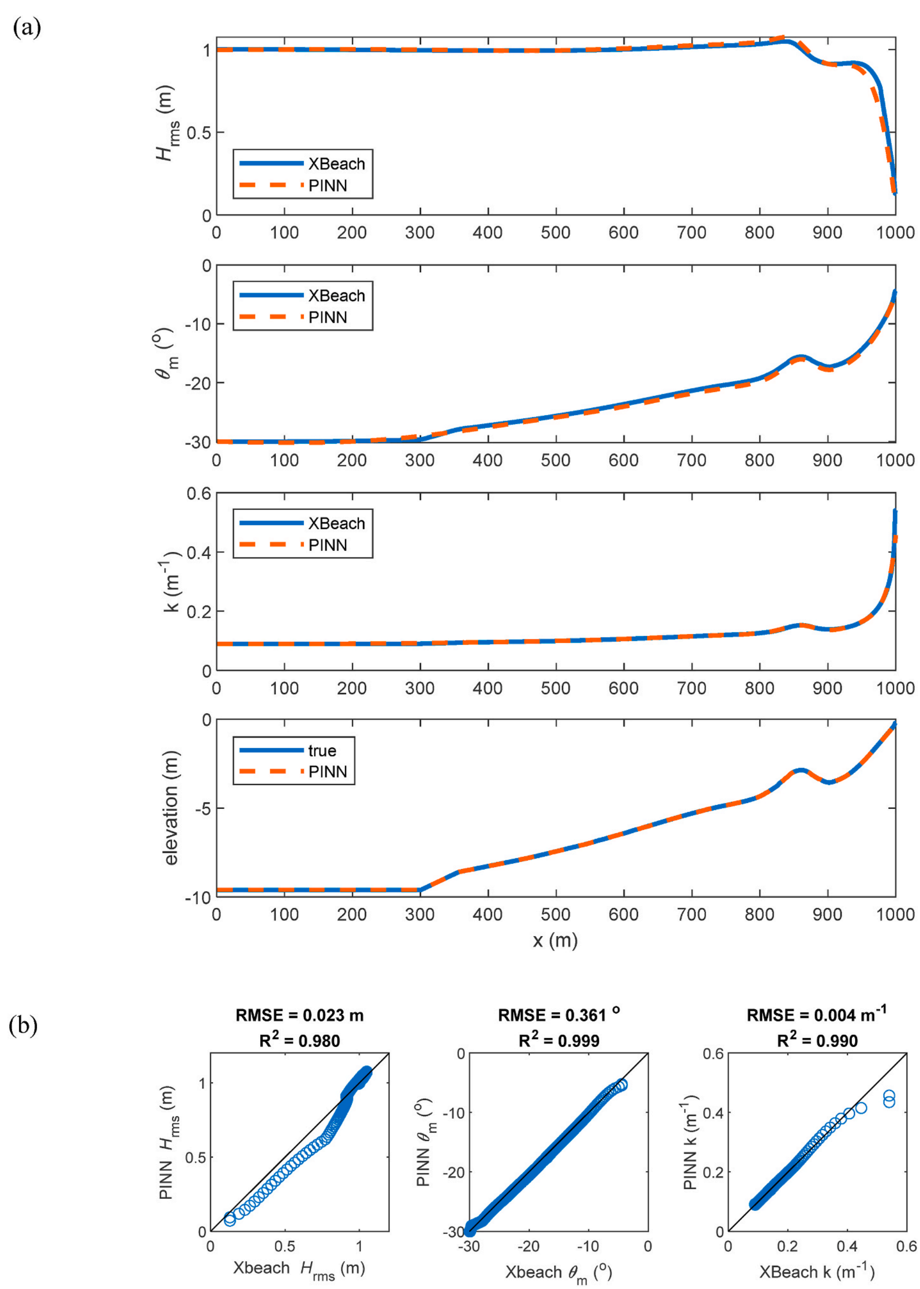

Fig. 4. Comparison between the XBeach and *NWnets* outputs over the alongshore uniform barred beach with incident waves of $m = 20$ (a) spatial variation of the predicted H_{rms}, θ_m, and k; (b) scatter plots of the predicted H_{rms}, θ_m, and k. The plots only contain testing data.

friction, and vegetation.

This study employed the numerical simulations of H_{rms} and θ_{m} from XBeach as training and testing data in the *NWnets* to reconstruct wave fields over the alongshore uniform barred beach for demonstration. Field observations should replace the simulation data for training and testing in applications. Physical processes of energy dissipation by vegetation and bottom friction were deactivated in XBeach because they were not included in the *NWnets*. The stationary mode of XBeach (version 5849) was implemented in the present study. Depth-induced wave breaking was calculated using the formulation from Battjes and Janssen (1978) with a constant breaker parameter $\gamma = 0.63$. The resolution in directional space ($d\theta$) was set to 1° in both XBeach and PINN models, covering the directional range from −90° to 90°. The specific wave boundary conditions applied in XBeach models can be found in Section 2.2.1. The grid resolution in the cross-shore direction was set to 1 m, leading to 1000 computational points in the XBeach simulation.

3. Results

3.1. *Wave field reconstruction over an alongshore uniform barred beach*

In this section, the outputs from XBeach and *NWnets* were compared to investigate the feasibility of using PINNs to reconstruct wave fields over an alongshore uniform barred beach. The comparison between the *NWnets* and XBeach outputs with incident waves of $m = 20$ is shown in Fig. 4. It can be observed that the *NWnets*-predicted H_{rms} and θ_{m} correlated well with the ones from XBeach. The error statistics were computed to quantify the prediction skills of the *NWnets*, including normalized root mean square error (*RMSE*) and R^2. Table 2 presents the relative test errors (Appendix) of the wave parameters simulated by the *NWnets* with different direction spreadings of incident waves. The results show that the simulation errors of *NWnets* are small for all test cases, indicating that the developed model has a satisfactory performance for reconstruction waves over the alongshore uniform barred beach. Better agreement can be found between the simulations from XBeach and *NWnets* when the directional spreading of incident waves is broader. This can be explained by the fact that a higher resolution of directional spreading is required in PINNs for reconstructing wave fields with narrow-banded waves, which will be further examined in Section 4.2.4. More discussions on the influence of the number of collocation points on the prediction performance of the *NWnets* will be presented in Section 4.2.2.

Table 2
Relative test errors of the *NWnets*-simulated H_{rms}, θ_m, and k on the alongshore uniform barred beach with different directional spreadings of incident waves.

m	Normalized *RMSE*				R^2 value		
	$\varepsilon_{H_{\mathrm{rms}}}$	$\varepsilon_{\theta_{\mathrm{m}}}$	ε_k	total ε	$R^2_{H_{\mathrm{rms}}}$	$R^2_{\theta_{\mathrm{m}}}$	R^2_k
8	0.019	0.012	0.031	0.062	0.984	0.995	0.996
20	0.025	0.012	0.044	0.081	0.980	0.999	0.990
32	0.025	0.014	0.051	0.090	0.977	0.999	0.989
130	0.030	0.014	0.089	0.133	0.960	0.998	0.949

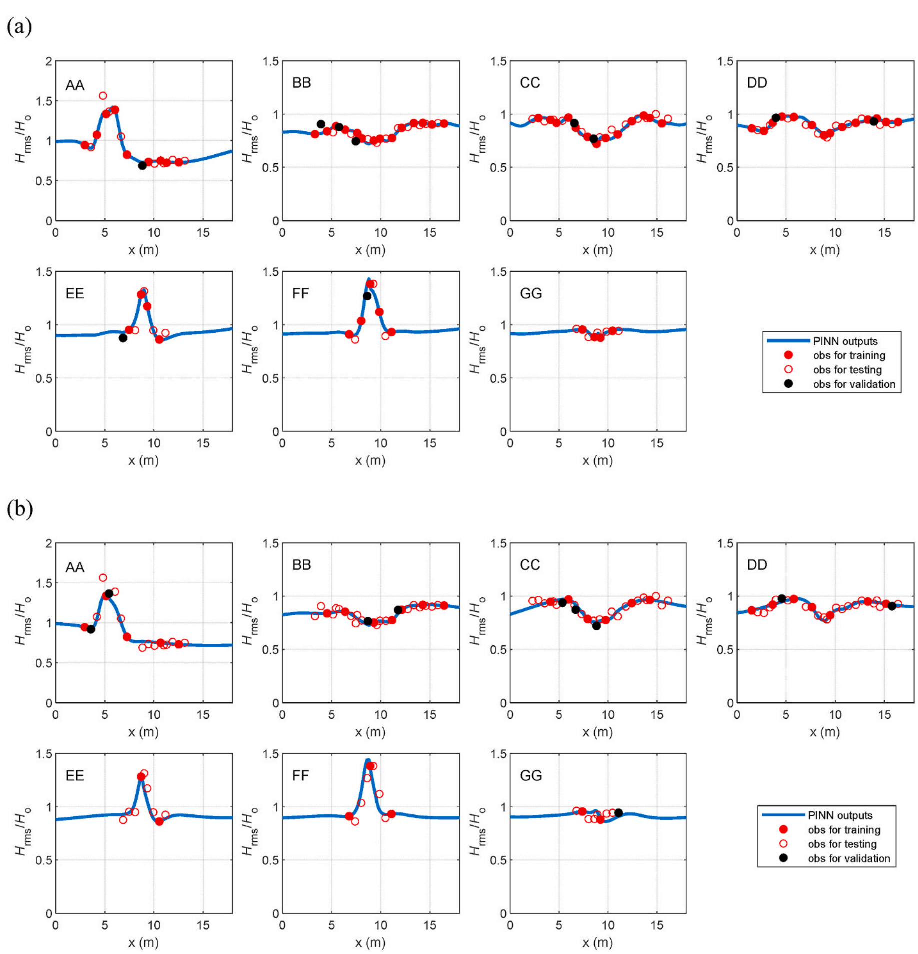

Fig. 5. Comparisons between experimental and PINN-simulated wave heights with (a) half of the wave height measurements used as training data; (b) a quarter of the wave height measurements used as training data.

3.2. Wave field reconstruction over a circular shoal

Fig. 5 shows the comparisons between the PINN-simulated and experimental data over a circular shoal. Solid lines represent the outputs from the *NWnets*, and circles are the measurements in the laboratory. The experimental data used for training and validating PINN models are shown by the red- and black-filled circles, respectively. The hollow circles represent the testing data for the model. When half of the wave height measurements were used for training (i.e., 63 training data), a good agreement could be found between the experimental and simulated wave heights (Fig. 5 (a) and Fig. 6 (a)). The simulation accuracy decreased when a quarter of the wave height measurements (i.e., 31 training points) were used as training data (Fig. 5 (b) and Fig. 6 (b)), but the *NWnets* could still capture the focusing of wave energy along the transects of *E-E* and *F–F* and the defocusing of wave energy along the transects of *C–C* and *D-D*. Table 3 shows the error statistics of the *NWnets* results when different numbers of wave height measurements were employed as the training data. Unsurprisingly, a better simulation performance could be obtained with more experimental data employed as training points.

Fig. 7 (a) and (b) present the spatial distributions of wave height simulated by the *NWnets* with 63 and 31 training points, respectively. It is seen that more details of wave field variation could be captured when more training data were applied in *NWnets.* However, both models can generate reasonable outputs and show the general pattern of wave field changes accurately. Specifically, it can be observed that the maximum wave height can reach up to 1.5 times the incident wave height along the transect *A-A*, and a decrease in wave height can be observed behind the shoal due to the defocusing of wave energy, consistent with the analysis of Chen et al. (2005). More testing cases are presented in the discussion section to further explore the factors influencing the spatial distribution

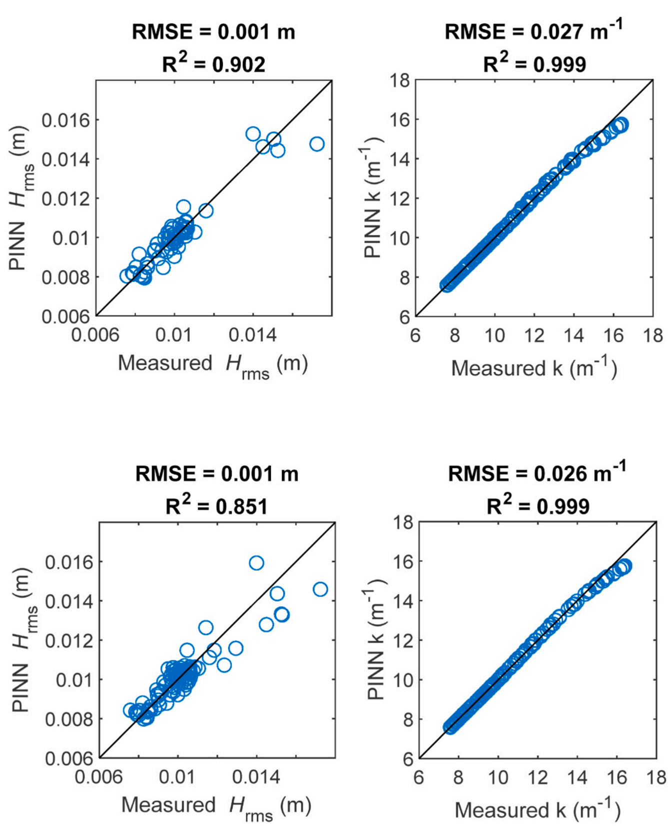

Fig. 6. Scatter plots of PINN-simulated and experimental data of H_{rms} and k with (a) half of the wave height measurements used as training data; (b) a quarter of the wave height measurements used as training data. The plots only contain testing data.

Table 3
Relative test errors of the *NWnets*-simulated H_{rms} and k with different numbers of wave height measurements used as training data.

# Training points	*RMSE*		R^2 value	
	H_{rms} (m)	k (m^{-1})	$R^2_{H_{\mathrm{rms}}}$	R^2_k
63 (50%)	0.0005	0.027	0.902	0.999
31 (25%)	0.0007	0.026	0.851	0.999
21 (16.7%)	0.0006	0.032	0.885	0.999
16 (12.5%)	0.0008	0.035	0.863	0.999

of wave heights simulated by the *NWnets*. Fig. 8 presents an example of weighting coefficients calculated by the adaptive learning rate algorithm with 63 wave height measurements employed as the training data. The convergence plot for the total loss function of *NWnets* shows that the training efforts are sufficient with Adam and L-BFGS-B in this study (Fig. 9).

4. Discussion

4.1. Comparison with conventional ANN

To examine the effect of physical regularization on the results, we generated a simulation using the conventional ANN model with 31 training points as an example (Fig. 10). The ANN model setup and hyperparameter selection were kept the same as the ones used in the *NWnets*, except that the total loss function only contained the measurement loss. The R^2 value for the predicted H_{rms} by the ANN decreased to 0.43, indicating that embedding the wave energy balance equation and dispersion relation into the networks indeed increases the simulation performance for reconstructing the wave field. It is seen that the largest errors of the conventional ANN model prediction appear along the transect *G-G* compared with the measurements (Fig. 10).

4.2. Training and prediction performance

Similar to the traditional ANN method, PINN results are achieved by solving nonconvex optimization problems, so there is no guarantee that PINNs can get unique solutions. In general, to obtain a good level of learning performance, some hyperparameters can be tuned by trial and error, such as activation functions, network structures, and the number of collocation points. In this section, the influence of network structures, the number of collocation points, the location of training data, and the resolution of directional spreading on simulation errors are discussed using the reconstruction of wave fields over the alongshore uniform barred beach as an example.

4.2.1. Influence of neural network sizes on test errors

The network structure has a crucial influence on the performance of PINNs. Based on Occam's razor theory (Blumer et al., 1987), it is preferable to achieve a network structure with the lowest number of layers and nodes and still enable effective training and generalizability. In order to determine such a network structure, we compared the results from the *NWnets* trained with different numbers of hidden layers and nodes. Table 4 shows the error statistics of the outputs from the *NWnets* for reconstructing the wave field over the alongshore uniform barred beach (m = 32) using different network structures (from 1 hidden layer of 10 nodes to 5 hidden layers of 40 nodes). It can be observed that the test error generally reduces when the model has more hidden layers and nodes per layer. Furthermore, there is no significant improvement in model accuracy by applying more than 4 layers of 30 nodes in the network structure. Considering simulation accuracy and computational cost, we employed the network structure of 4 hidden layers of 30 nodes to reconstruct both wave fields over the barred beach and circular shoal in this study. It is worth mentioning that the optimal network size is case-dependent. For example, a deeper and wider network may be

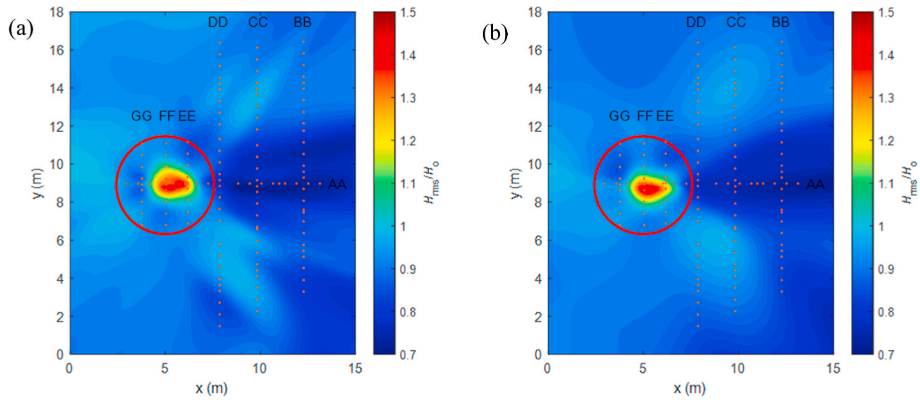

Fig. 7. The spatial distribution of wave height simulated by *NWnets* with (a) half of the wave height measurements used as training data; (b) a quarter of the wave height measurements used as training data.

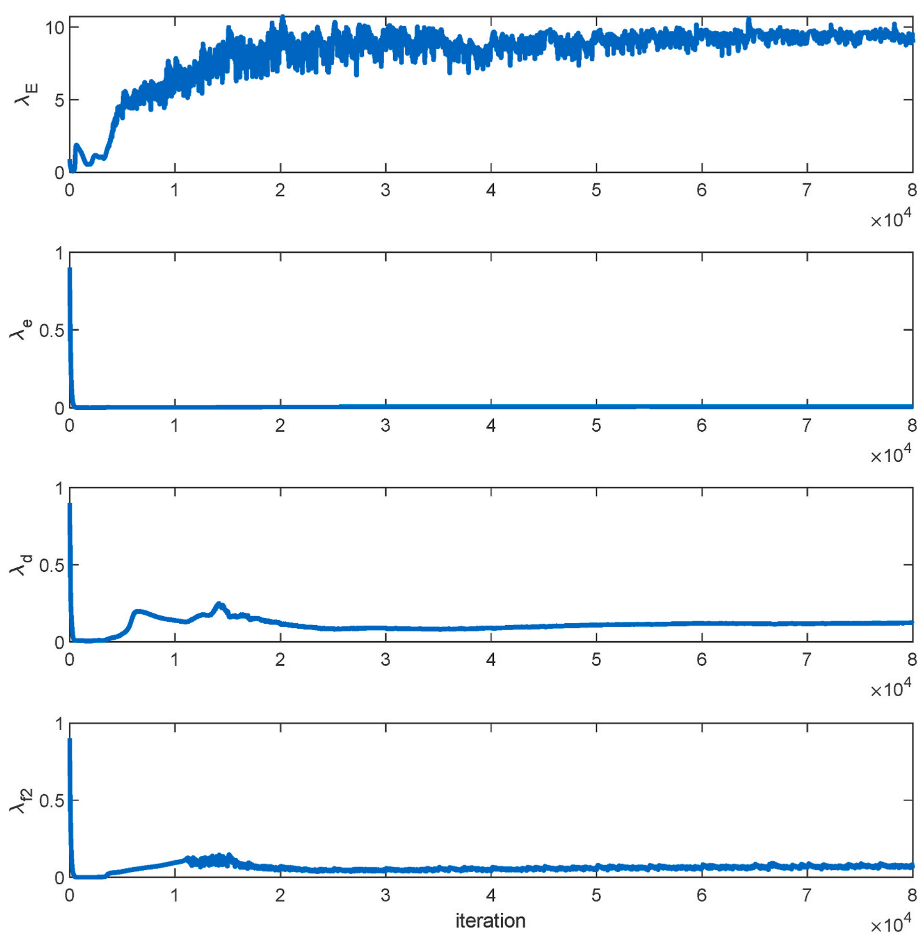

Fig. 8. The weighting coefficients calculated by the adaptive learning rate annealing algorithm during the training iterations with Adam for reconstructing wave fields over the circular shoal with 63 wave height measurements used as training data.

required to achieve better accuracy for simulating a stiff system. Although the optimal network size can be case-dependent, our results indicate that the PINN outputs are not overly sensitive to the network sizes in this study.

4.2.2. Influence of collocation points on test errors

To determine the influence of collocation points on the learning performance of the *NWnets*, we compared the error statistics of PINN outputs with different numbers of collocation points applied during training. Fig. 11 shows the total normalized *RMSE* of PINN outputs against different numbers of collocation points over the alongshore uniform barred beach. The collocation points were uniformly distributed over the entire computational domain from x = 1–1000 m. Unsurprisingly, the total normalized *RMSE* decreases when the number of collocation points increases. However, the computational cost increases when more collocation points are employed during training. In this study, 1000 collocation points were used in the *NWnets* for reconstructing wave fields over the alongshore unformed barred beach, considering both simulation accuracy and computational cost.

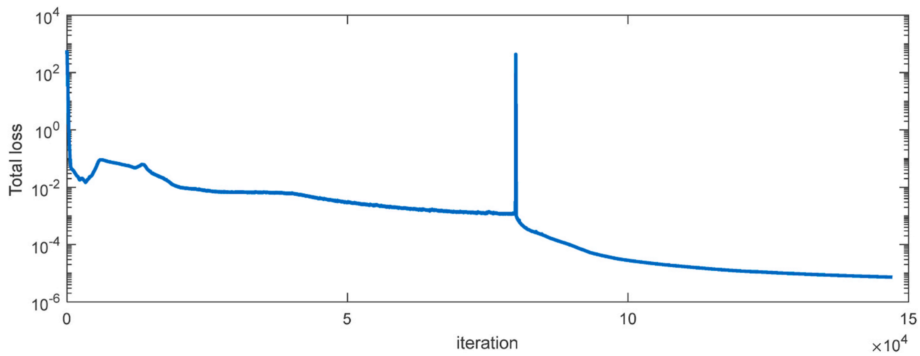

Fig. 9. The convergence of total loss function when 63 wave height measurements were used as training data.

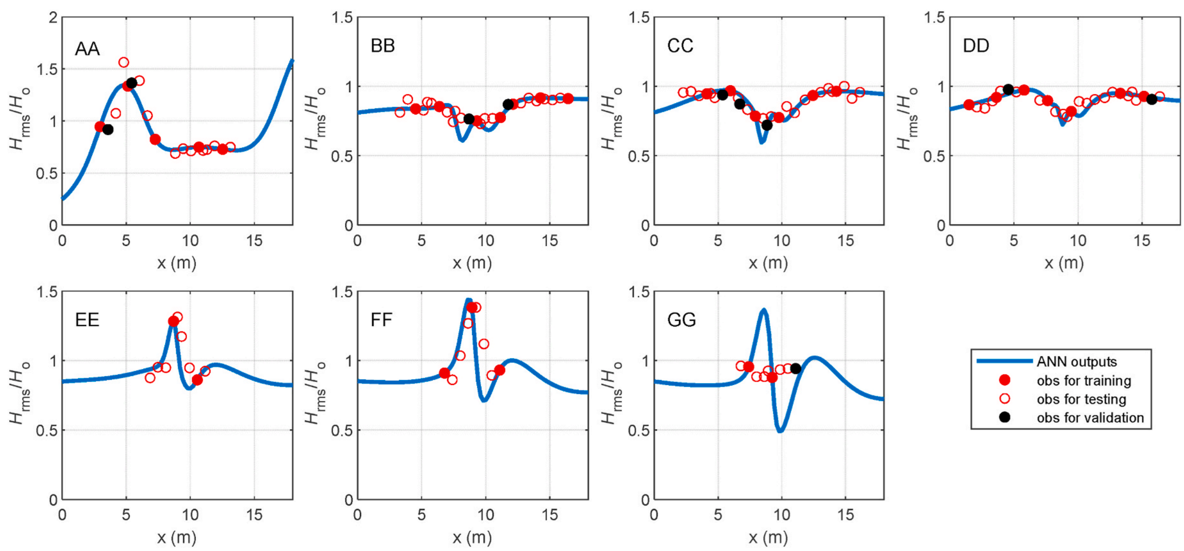

Fig. 10. Comparisons between experimental and conventional ANN-simulated wave heights with a quarter of the wave height measurements used as training data.

Table 4
Error statistics of the *NWnets*-simulated H_{rms}, θ_m, and k with different network structures.

Neural network size	Normalized *RMSE*			R^2 value		
	ε_{H_s}	ε_{θ_m}	ε_k	$R^2_{H_s}$	$R^2_{\theta_m}$	R^2_k
1 × 10	0.051	0.025	0.156	0.860	0.991	0.910
1 × 20	0.027	0.060	0.133	0.963	0.995	0.931
1 × 30	0.027	0.057	0.089	0.974	0.997	0.970
1 × 40	0.026	0.026	0.111	0.976	0.998	0.951
2 × 10	0.025	0.023	0.089	0.975	0.998	0.970
2 × 20	0.026	0.031	0.111	0.972	0.998	0.949
2 × 30	0.025	0.009	0.067	0.979	0.999	0.982
2 × 40	0.026	0.010	0.067	0.974	0.999	0.984
3 × 10	0.023	0.015	0.078	0.981	1.000	0.978
3 × 20	0.026	0.015	0.078	0.976	0.999	0.979
3 × 30	0.025	0.010	0.044	0.977	0.999	0.992
3 × 40	0.029	0.038	0.111	0.967	0.998	0.953
4 × 10	0.025	0.023	0.089	0.977	0.998	0.967
4 × 20	0.025	0.015	0.111	0.976	0.999	0.952
4 × 30	**0.025**	**0.008**	**0.056**	**0.977**	**0.999**	**0.989**
4 × 40	0.026	0.016	0.067	0.974	0.999	0.983
5 × 10	0.025	0.016	0.122	0.973	0.997	0.946
5 × 20	0.024	0.010	0.056	0.979	0.999	0.987
5 × 30	0.025	0.011	0.078	0.978	0.999	0.978
5 × 40	0.024	0.017	0.044	0.979	0.998	0.993

4.2.3. *Influence of training points on test errors*

The sensitivity of the performance of *NWnets* regarding the training points of H_{rms} is discussed in this section. On the alongshore uniform barred beach, when the offshore wave condition is $H_{\mathrm{rms}} = 1$ m and $T_{\mathrm{p}} = 8$ s, the shoaling zone extends from about $x = 0$–700 m, and the surf zone covers the domain from about $x = 700$–1000 m. Thus, the training data of H_{rms} can be correspondingly classified into two categories based on the locations of points (i.e., inside surf zone or outside surf zone). In the previous analysis, three training points of H_{rms} (at $x = 100$, 500, 900 m. i.e., two outside surf zone and one inside surf zone) were employed for reconstructing the wave fields over the barred beach, and reasonable

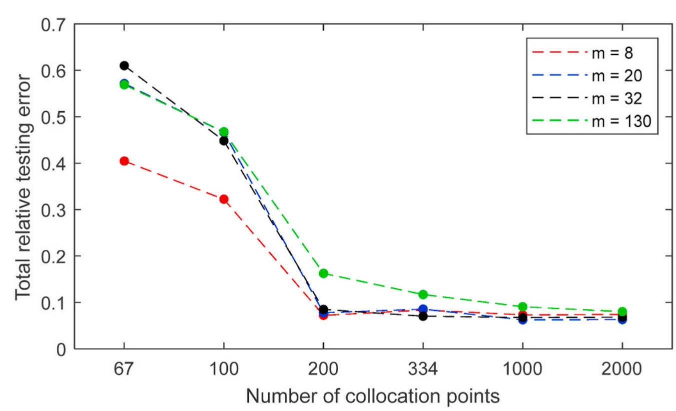

Fig. 11. Total normalized *RMSE* of PINN outputs against different numbers of collocation points applied in the *NWnets* for reconstructing wave fields over the alongshore uniform barred beach.

results could be obtained for both broad- and narrow-banded waves. Here, the performance of *NWnets* was examined using different training points of H_{rms} in the model. The training point of the mean wave angle was fixed at $x = 300$ m. Table 5 shows the error statistics of PINN outputs when the training data of H_{rms} were located at (i) $x = 100$, 300, 600 m (i.e., all three training points outside surf zone), (ii) $x = 300$, 900, 950 m (i.e., two inside surf zone and one outside surf zone), and (iii) x = 300, 900 m (i.e., one inside surf zone and one outside surf zone). The results indicate that the location of H_{rms} training points has a limited influence on the performance of the *NWnets*. Moreover, even two training points of H_{rms} can be sufficient to reconstruct wave fields with the *NWnets* when $m = 8$, 20, and 32.

4.2.4. Influence of directional resolution $d\theta$ on test errors

In the above analysis, the resolution of directional spreading of waves was set to 1° in both XBeach and PINN models for simulating wave propagation over the alongshore uniform barred beach. To examine the influence of the width of directional bins on PINN results, the wave parameters were simulated using different values of $d\theta$ in *NWnets* and XBeach, including $d\theta = 0.5°$, 3°, 5°, 7°, and 10°. Table 6 shows that the resolution of directional spreading has a limited impact on the simulation accuracy of *NWnets* for broad-banded waves (i.e., m = 8). For narrow-banded waves, however, the prediction skill decreases when the value of $d\theta$ is large. For example, the total normalized *RMSE* goes up to about 0.3 when $d\theta$ is 10° for narrow-banded waves with $m =$ 32 and 130. When the width of direction bins decreases to 0.5°, the total normalized *RMSE* drops to about 0.1. Even smaller simulation errors could be expected if the resolution of the directional spreading is further increased, although it might be computationally expensive to do so with the *NWnets*. Overall, the width of direction bins should be sufficiently small so that the directional space can be well resolved for simulating narrow-banded waves with PINNs.

4.3. Strategies for improving simulation accuracy of the NWnets

Though the current results are encouraging, some potential methods can be utilized to increase the simulation accuracy of the *NWnets* for reconstructing wave fields. Firstly, we can integrate more physics in PINNs to describe the wave field more realistically. The physical laws incorporated into the current version of *NWnets* may not fully capture the physics of the wave field over the circular shoal. For instance, the wave interference caused by the combined refraction and diffraction was not included in the *NWnets*. The reason why the model can still reconstruct the wave field with high accuracy in this study is that the wave interference effect behind the circular shoal was suppressed due to the broad-banded incident waves and wave dissipation. However, wave interference can be strong behind the shoal for the wave field with narrow-banded incident waves. Thus, an additional source term regarding quasi-coherent theory needs to be included in the *NWnets* to account for wave interference caused by the combined refraction and diffraction (Smit et al., 2015). From another perspective, the simulation accuracy can be simply improved by using more training data. The result shows that when all available wave height measurements are applied as the training points, the outputs from *NWnets* capture more details of the wave field variation behind the shoal (Fig. 12). This indicates that even though the wave coherent effects are not included in the model, PINN outputs may still present the wave interference feature when more training points are applied. Further studies can be conducted to validate whether using less training data can achieve a good simulation of wave fields when the additional term regarding quasi-coherent theory is included in the *NWnets*.

Table 5
Error statistics of the simulated H_{rms}, θ_m, and k with different training points of H_{rms} applied in the *NWnets*.

Training points location for H_{rms}	m	Normalized *RMSE*			R^2 value		
		$\varepsilon_{H_{rms}}$	ε_{θ_m}	ε_k	$R^2_{H_{rms}}$	$R^2_{\theta_m}$	R^2_k
100, 300, 600	8	0.020	0.053	0.073	0.980	0.981	0.977
	20	0.023	0.030	0.041	0.980	0.998	0.993
	32	0.026	0.049	0.087	0.972	0.996	0.971
	130	0.026	0.049	0.087	0.972	0.996	0.971
300, 900, 950	8	0.024	0.038	0.039	0.957	0.983	0.994
	20	0.022	0.023	0.063	0.974	0.996	0.984
	32	0.022	0.042	0.087	0.979	0.998	0.968
	130	0.024	0.005	0.068	0.979	1.000	0.981
300, 900	8	0.029	0.061	0.040	0.947	0.971	0.994
	20	0.027	0.020	0.044	0.973	0.998	0.992
	32	0.027	0.013	0.038	0.976	0.999	0.994
	130	0.042	0.024	0.122	0.945	0.995	0.941

4.4. Transfer learning of the NWnets

Similar to numerical simulations with conventional physics-based models, we need to train the *NWnets* again when wave boundary conditions or bathymetry change. To accelerate the training process of PINNs, transfer learning methods can be utilized when the following simulation has slightly different wave boundary conditions or bathymetry (e.g., Kissas et al., 2020). Specifically, instead of training a new network from scratch, the pretrained networks can be used to initialize the subsequent simulations (Jin et al., 2021). For example, assuming that the *NWnets* for reconstructing wave fields over the alongshore uniform barred beach have been well developed with the boundary condition of $H_{rms} = 1$ m and $T_p = 8$ s, then we would like to simulate the wave field with a different wave boundary condition of $H_{rms} = 0.8$ m and $T_p = 10$ s. What we can do is to initialize the new network weights and bias using the parameters of the pretrained *NWnets* with the boundary condition of $H_{rms} = 1$ m and $T_p = 8$ s. Then, the second network parameters are further tuned based on the new boundary conditions of $H_{rms} = 0.8$ m and $T_p = 10$ s. As a result, the computational efficiency of the subsequent simulation can be improved. Only L-BFGS-B was employed during the training processes in transfer learning because the initialization was already close to the solution.

In this study, based on the well-trained PINN model with the original bathymetry and boundary conditions of $H_{rms} = 1$ m and $T_p = 8$ s, transfer learning techniques were applied to reconstruct wave fields with (i) a new wave boundary condition of $H_{rms} = 0.8$ m and $T_p = 10$ s; and (ii) a new bathymetry with 2 bars over the alongshore uniform barred beach (Fig. 13). Table 7 presents the error statistics of the wave parameters simulated with and without the transfer learning method. The results show that the PINN models with transfer learning have higher simulation accuracy and computational efficiency than those without using transfer learning techniques. This is because wave fields over the alongshore unformed barred beach are similar when the bathymetry or wave boundary conditions are slightly different. As a result, improved prediction performance and convergence speed can be achieved with better-initialized network parameters.

4.5. PINNs vs. traditional physics-based nearshore models

Admittedly, PINN models are not expected to replace traditional physics-based nearshore models, which have been developed and successfully used for decades. For instance, the convergence of PINNs is not always guaranteed because of the non-convexity of the neural network optimization (Sun et al., 2020), and PINNs may generate less accurate results for predicting overly complicated systems when only a few training points are available. Also, the training (e.g., architecture) of PINNs is case-specific, so the *NWnets* can be less generically applicable than physics-based models. However, the development of *NWnets* for surrogate modeling presents some promising capabilities. For example, the *NWnets* can solve ill-posed problems without accurate wave conditions at the open boundary and avoid generating cumbersome

Table 6
Error statistics of *NWnets* outputs simulated with different values of $d\theta$ over the alongshore uniform barred beach.

$d\theta$ (deg)		Normalized *RMSE*				R^2 value		
		$\varepsilon_{H_{rms}}$	ε_{θ_m}	ε_k	total ε	$R^2_{H_{rms}}$	$R^2_{\theta_m}$	R^2_k
10	m = 8	0.019	0.022	0.038	0.079	0.982	0.996	0.995
	m = 20	0.118	0.059	0.018	0.195	0.738	0.895	0.999
	m = 32	0.151	0.112	0.044	0.308	0.671	0.634	0.992
	m = 130	0.242	0.071	0.036	0.349	0.405	0.912	0.995
7	m = 8	0.019	0.020	0.034	0.074	0.982	0.973	0.995
	m = 20	0.024	0.011	0.034	0.069	0.980	0.999	0.995
	m = 32	0.025	0.019	0.062	0.107	0.983	0.996	0.985
	m = 130	0.168	0.171	0.046	0.384	0.652	0.747	0.991
5	m = 8	0.019	0.013	0.028	0.060	0.983	0.999	0.997
	m = 20	0.023	0.011	0.046	0.079	0.980	0.999	0.992
	m = 32	0.025	0.006	0.032	0.063	0.978	1.000	0.996
	m = 130	0.040	0.059	0.059	0.158	0.959	0.999	0.985
3	m = 8	0.019	0.022	0.048	0.089	0.984	0.996	0.991
	m = 20	0.025	0.009	0.049	0.083	0.977	0.999	0.990
	m = 32	0.025	0.014	0.078	0.117	0.978	0.999	0.977
	m = 130	0.032	0.009	0.099	0.140	0.963	0.999	0.962
0.5	m = 8	0.020	0.026	0.039	0.084	0.982	0.993	0.994
	m = 20	0.022	0.014	0.039	0.075	0.981	0.999	0.993
	m = 32	0.025	0.008	0.046	0.078	0.978	1.000	0.992
	m = 130	0.029	0.009	0.098	0.136	0.971	0.999	0.962

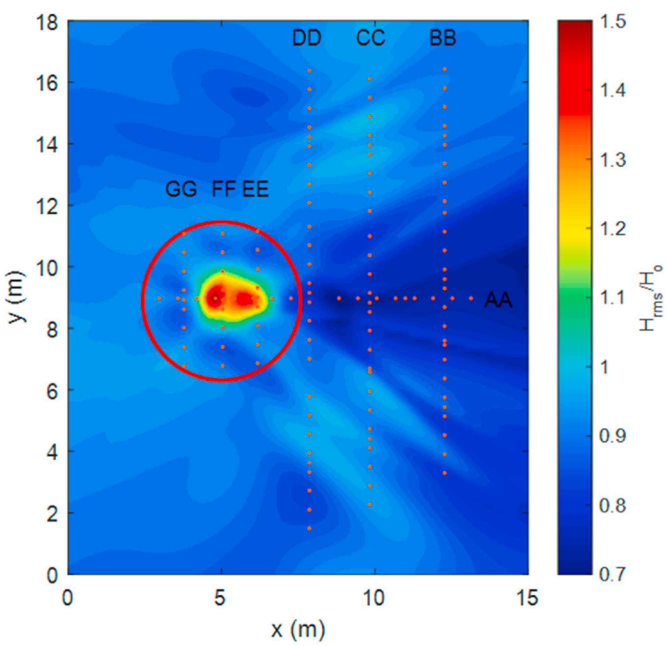

Fig. 12. The spatial distribution of wave height simulated by the *NWnets* with all the wave height measurements applied as training data.

computational meshes for complicated geometries, which is highly desirable when the rapid prediction of wave fields is needed in many applications. For instance, the *NWnets* could be employed to rapidly reconstruct the wave fields in field experiments where a limited number of wave gages were deployed nearshore, such as the Scripps Canyon Experiment (Gorrell et al., 2011).

It is worth mentioning that PINNs have the ability to discover equations or parametrizations (e.g., Pfister et al., 2019; Huang et al., 2020; Chen et al., 2021). For example, in coastal engineering applications, PINNs could be used to determine higher-order dispersive terms in Boussinesq-type equations, or discover sub-grid scale turbulence mixing terms for large eddy simulation models (e.g., Zanna and Bolton, 2020). Another advantage of PINN models is to solve inverse problems, such as the depth inversion problem. Unlike the conventional data assimilation method, PINNs do not require simulations from deterministic forward

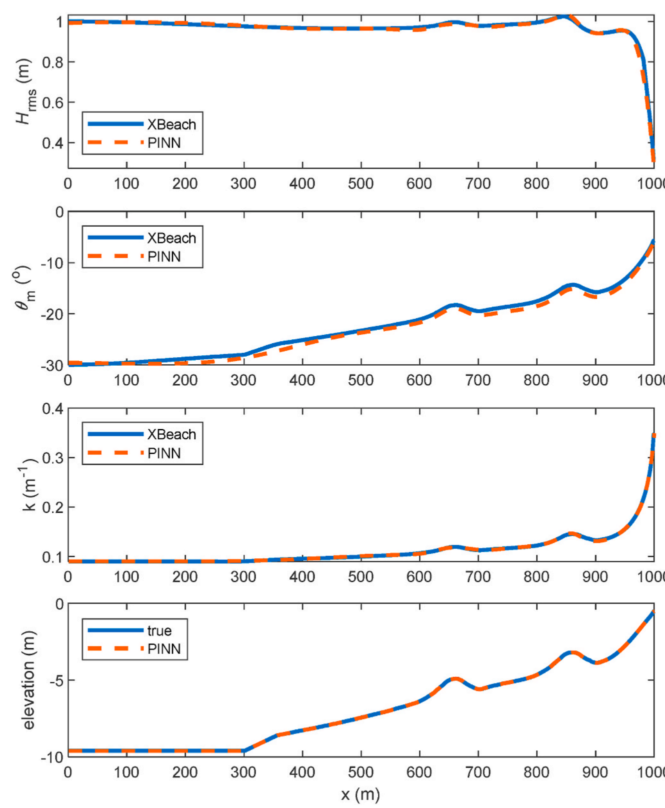

Fig. 13. Comparison between XBeach and PINN outputs over the alongshore uniform beach with 2 bars using transfer learning techniques.

numerical models or knowledge about the uncertainty of observations and the uncertainty of the numerical model (Wilson et al., 2014). Thus, applying PINNs to obtain the solution to inverse problems would be desirable because PINNs can execute much faster than data assimilation algorithms without running thousands or millions of forward model simulations for evaluating estimators and characterizing posterior distributions of parameters. Further analysis should be carried out to examine the performance of PINNs for solving equation discovery and depth inversion problems.

Table 7
Error statistics of the simulated wave parameters from the *NWnets* with and without the transfer learning method over the alongshore uniform barred beach.

		Normalized *RMSE*			R^2 value			Computational cost (Number of iterations)
		$\varepsilon_{H_{\mathrm{rms}}}$	$\varepsilon_{\theta_{\mathrm{m}}}$	ε_k	$R^2_{H_{\mathrm{rms}}}$	$R^2_{\theta_{\mathrm{m}}}$	R^2_k	
New wave boundary condition	w/transfer learning	0.007	0.016	0.027	0.994	0.999	0.996	20k L-BFGS-B
	w/o transfer learning	0.026	0.024	0.029	0.882	0.996	0.995	40k Adam + 120k L-BFGS-B
New bathymetry	w/transfer learning	0.010	0.022	0.009	0.987	0.996	0.999	50k L-BFGS-B
	w/o transfer learning	0.009	0.021	0.012	0.988	0.996	0.999	40k Adam + 120k L-BFGS-B

5. Summary and conclusions

In the past two decades, many soft-computing models have been proposed to study nonlinear relationships between input features and labels in coastal engineering applications. However, the direct use of pure data-driven models often encounters difficulties in applications because of their enormous data demands, poor generalizability to out-of-sample cases, and a lack of the ability to generate physically consistent results with limited data. This study proposed a novel composite PINN model, the *NWnets*, to reconstruct wave fields in the nearshore with limited wave measurements by incorporating the prior knowledge of wave mechanics (i.e., wave energy balance equation and dispersion relation) into the soft-computing deep learning algorithm. The equations were formulated with the fully-connected neural networks, and automatic differentiation was employed to represent all the differential operators in the energy balance equation. The effectiveness of the *NWnets* was explored by reconstructing wave fields over a two-dimensional alongshore uniform barred beach and a three-dimensional circular shoal.

Firstly, the wave fields with narrow- and broad-banded incident waves (i.e., $m = 8$, 20, 32, and 130) were simulated with the *NWnets* over an alongshore uniform barred beach. The results indicate that the simulations of H_{rms} and θ_{m} from the *NWnets* correlated well with those from XBeach when only three wave height measurements were applied as training data. Moreover, the *NWnets* can reconstruct the entire wave field and capture the focusing and defocusing of wave energy over a circular shoal with laboratory measurements of wave height employed as training data. Since the simulation errors are small for all test cases, the *NWnets* show a remarkable ability to reconstruct spatial variations of wave fields in the nearshore with limited measurements.

Furthermore, this work investigated the influences of network sizes, numbers of collocation points, locations of training points, and the resolution of wave directional spreading on the performance of the *NWnets*. It was found that the wave field over the alongshore uniform barred beach can be well reconstructed with proper neural network architectures. Considering the simulation accuracy and computational cost, we used the network structure of 4 hidden layers of 30 nodes to reconstruct both wave fields over the barred beach and circular shoal in this study. Additionally, we compared the error statistics of the *NWnets* outputs when different numbers of collocation points were applied in the model. Unsurprisingly, the total normalized *RMSE* decreases when the number of collocation points increases, while the computational cost increases when more collocation points are utilized during training. The results indicate that the locations of H_{rms} training points have a limited influence on the simulation accuracy of *NWnets*. Even two training points of H_{rms} are sufficient to reconstruct wave fields with broad-banded incident waves on an alongshore uniform beach by the *NWnets*. Moreover, it was found that the resolution of directional spreading has a limited impact on the simulation accuracy of *NWnets* for broad-banded incident waves (i.e., m = 8). While for narrow-banded waves, the prediction skill of *NWnets* decreases when $d\theta$ gets larger. Thus, the width of direction bins should be sufficiently small so that the directional space can be well resolved for simulating narrow-banded waves with PINNs.

Overall, the advantages of PINN models are attributed to the fact that encoding prior knowledge during the training process can constrain learning and compensate for the insufficiency of observational data. Therefore, such models can generalize well and provide reliable results even when only limited training data are available. This study is the first attempt to investigate the capability of PINNs for reconstructing wave fields in the nearshore with scarce wave measurements. Though the current results are encouraging, many open questions still exist. For example, what is the accuracy of using PINN models to solve inverse problems, such as estimating water depth based on measured wave parameters in nearshore regions? Can PINN models be utilized to determine the friction coefficient or wave breaking parameters in nearshore models accurately? More studies will be carried out to answer those questions and further test the performance of the *NWnets* under storm conditions.

CRediT authorship contribution statement

Nan Wang: Methodology, Software, Writing – original draft. **Qin Chen:** Conceptualization, Methodology, Validation, Writing – review & editing, Supervision, Funding acquisition. **Zhao Chen:** Investigation, Resources, Writing – review & editing.

Declaration of competing interest

The authors declare that they have no known competing financial interests or personal relationships that could have appeared to influence the work reported in this paper.

Acknowledgments

Funding for the study has been provided by the U.S. National Science Foundation (NSF Grants 1856359 and 2139882). Any use of trade, firm, or product names is for descriptive purposes only and does not imply endorsement by the U.S. Government.

Appendix

Error metrics

Statistical measures shown below were used to quantify the skills of the developed models.
RMSE:

$$RMSE = \sqrt{\frac{\sum_i^N (y_i - \hat{y}_i)^2}{N}} \tag{A.1}$$

R^2:

$$R^2 = \left(\frac{\sum_i^N (y_i - \hat{y}_i)^2}{\sqrt{\sum_i^N (y_i - \overline{y}_i)^2 \sum_i^N (\hat{y}_i - \overline{\hat{y}}_i)^2}} \right)^2 \tag{A.2}$$

Normalized $RMSE$ of H_{rms}:

$$\varepsilon_{H_{\mathrm{rms}}} = \frac{RMSE_{H_{\mathrm{rms}}}}{\Delta H_{\mathrm{rms}}} \tag{A.3}$$

Normalized $RMSE$ of θ_{m}:

$$\varepsilon_{\theta_m} = \frac{RMSE_{\theta_{\mathrm{m}}}}{\Delta \theta_{\mathrm{m}}} \tag{A.4}$$

Normalized $RMSE$ of k:

$$\varepsilon_k = \frac{RMSE_k}{\Delta k} \tag{A.5}$$

in which N is the number of samples, $\hat{y}_i$ is the estimated values and y_i is the true value. ΔH_{rms}, $\Delta\theta_{\mathrm{m}}$, and Δk were used to normalize the $RMSE$, equal to 1 m, 30°, and 0.09 m^{-1}, respectively. These values correspond to the incident wave condition at the offshore boundary of the longshore uniform barred beach.

References

Battjes, J.A., Janssen, J., 1978. Energy loss and set-up due to breaking of random waves. in: Coast. Eng. 569–587, 1978.

Bento, P.M.R., Pombo, J.A.N., Mendes, R.P.G., Calado, M.R.A., Mariano, S., 2021. Ocean wave energy forecasting using optimised deep learning neural networks. Ocean Eng 219, 108372.

Blumer, A., Ehrenfeucht, A., Haussler, D., Warmuth, M.K., 1987. Occam's razor. Inf. Process. Lett. 24, 377–380.

Booij, N., Ris, R.C., Holthuijsen, L.H., 1999. A third-generation wave model for coastal regions: 1. Model description and validation. J. Geophys. Res. Ocean. 104, 7649–7666.

Brown, J.M., 2010. A case study of combined wave and water levels under storm conditions using WAM and SWAN in a shallow water application. Ocean Model. 35, 215–229.

Chawla, A., Özkan-Haller, H.T., Kirby, J.T., 1998. Spectral model for wave transformation and breaking over irregular bathymetry. J. Waterw. Port, Coast. Ocean Eng. 124, 189–198.

Chawla, A.K., Kirby, J.T., Delaware., U. of, Engineering., D. of C., Delaware., U. of, Research., C. for A.C., Delaware., U. of, Laboratory., O.E, 1996. Wave Transformation over a Submerged Shoal. University of Delaware, Dept. of Civil Engineering, Center for Applied Coastal Research, Newark, Del.

Chen, Q., Kirby, J.T., Dalrymple, R.A., Kennedy, A.B., Chawla, A., 2000. Boussinesq modeling of wave transformation, breaking, and runup. II: 2D. J. Waterw. Port, Coast. Ocean Eng. 126, 48–56. https://doi.org/10.1061/(ASCE)0733–950X(2000)126:1(48).

Chen, Q., Zhao, H., Hu, K., Douglass, S.L., 2005. Prediction of wind waves in a shallow estuary. J. Waterw. Port, Coast. Ocean Eng. 131 https://doi.org/10.1061/(ASCE)0733–950X(2005)131:4(137).

Chen, Z., Liu, Y., Sun, H., 2022. Forecasting of nonlinear dynamics based on symbolic invariance. Comput. Phys. Commun. 277, 108382.

Chen, Z., Liu, Y., Sun, H., 2021. Physics-informed learning of governing equations from scarce data. Nat. Commun. 12, 1–13.

Chen, Z., Sun, H., 2021. Sparse representation for damage identification of structural systems. Struct. Health Monit. 20, 1644–1656.

Cornejo-Bueno, L., Nieto-Borge, J.C., García-Díaz, P., Rodríguez, G., Salcedo-Sanz, S., 2016. Significant wave height and energy flux prediction for marine energy applications: a grouping genetic algorithm - extreme Learning Machine approach. Renew. Energy 97. https://doi.org/10.1016/j.renene.2016.05.094.

Deo, M.C., Jha, A., Chaphekar, A.S., Ravikant, K., 2001. Neural networks for wave forecasting. Ocean Eng 28. https://doi.org/10.1016/S0029-8018(00)00027-5.

Deo, M.C., Naidu, C.S., 1998. Real time wave forecasting using neural networks. Ocean Eng 26, 191–203.

Elbisy, M.S., Elbisy, A.M.S., 2021. Prediction of significant wave height by artificial neural networks and multiple additive regression trees. Ocean Eng 230, 109077.

Glorot, X., Bengio, Y., 2010. Understanding the difficulty of training deep feedforward neural networks. In: Proceedings of the Thirteenth International Conference on Artificial Intelligence and Statistics, pp. 249–256.

Gorrell, L., Raubenheimer, B., Elgar, S., Guza, R.T., 2011. SWAN predictions of waves observed in shallow water onshore of complex bathymetry. Coast. Eng. 58, 510–516.

Hasselmann, K., Hasselmann, S., Bauer, E., Janssen, P.A.E.M., Komen, G.J., Bertotti, L., Lionello, P., Guillaume, A., Cardone, V.C., Greenwood, J.A., Reistad, M., Zambresky, L., Ewing, J.A., 1988. The WAM model - a third generation ocean wave prediction model. J. PHYS. Ocean. 18 https://doi.org/10.1175/1520-0485(1988)018<1775:twmtgo>2.0.co;2.

Holthuijsen, L.H., Booij, N., Herbers, T.H.C., 1989. A prediction model for stationary, short-crested waves in shallow water with ambient currents. Coast. Eng. 13, 23–54.

Huang, Z., Tian, Y., Li, C., Lin, G., Wu, L., Wang, Y., Jiang, H., 2020. Data-driven automated discovery of variational laws hidden in physical systems. J. Mech. Phys. Solid. 137, 103871.

Jain, P., Deo, M.C., Latha, G., Rajendran, V., 2011. Real time wave forecasting using wind time history and numerical model. Ocean Model. 36 https://doi.org/10.1016/j.ocemod.2010.07.006.

James, S.C., Zhang, Y., O'Donncha, F., 2018. A machine learning framework to forecast wave conditions. Coast. Eng. 137 https://doi.org/10.1016/j.coastaleng.2018.03.004.

Janssen, T.T., Battjes, J.A., 2007. A note on wave energy dissipation over steep beaches. Coast. Eng. 54, 711–716.

Jia, X., Willard, J., Karpatne, A., Read, J., Zwart, J., Steinbach, M., Kumar, V., 2019. Physics guided RNNs for modeling dynamical systems: a case study in simulating lake temperature profiles. In: Proceedings of the 2019 SIAM International Conference on Data Mining, pp. 558–566.

Jin, X., Cai, S., Li, H., Karniadakis, G.E., 2021. NSFnets (Navier-Stokes flow nets): physics-informed neural networks for the incompressible Navier-Stokes equations. J. Comput. Phys. 426, 109951.

Jörges, C., Berkenbrink, C., Stumpe, B., 2021. Prediction and reconstruction of ocean wave heights based on bathymetric data using LSTM neural networks. Ocean Eng 232, 109046.

Karniadakis, G.E., Kevrekidis, I.G., Lu, L., Perdikaris, P., Wang, S., Yang, L., 2021. Physics-informed machine learning. Nat. Rev. Phys. 3, 422–440.

Karpatne, A., Atluri, G., Faghmous, J.H., Steinbach, M., Banerjee, A., Ganguly, A., Shekhar, S., Samatova, N., Kumar, V., 2017. Theory-guided data science: a new paradigm for scientific discovery from data. IEEE Trans. Knowl. Data Eng. 29, 2318–2331.

Kingma, D.P., Ba, J., 2014. Adam: A Method for Stochastic Optimization arXiv Prepr. arXiv1412.6980.

Kissas, G., Yang, Y., Hwuang, E., Witschey, W.R., Detre, J.A., Perdikaris, P., 2020. Machine learning in cardiovascular flows modeling: predicting arterial blood pressure from non-invasive 4D flow MRI data using physics-informed neural networks. Comput. Methods Appl. Mech. Eng. 358, 112623.

Kurapov, A.L., Egbert, G.D., Allen, J.S., Miller, R.N., 2007. Representer-based variational data assimilation in a nonlinear model of nearshore circulation. J. Geophys. Res. Ocean. 112.

Lee, J.-W., Irish, J.L., Bensi, M.T., Marcy, D.C., 2021. Rapid prediction of peak storm surge from tropical cyclone track time series using machine learning. Coast. Eng. 170, 104024.

Liu, D.C., Nocedal, J., 1989. On the limited memory BFGS method for large scale optimization. Math. Program. 45, 503–528.

Lu, L., Meng, X., Mao, Z., Karniadakis, G.E., 2021. DeepXDE: a deep learning library for solving differential equations. SIAM Rev. 63, 208–228.

Lynett, P.J., Wu, T.-R., Liu, P.L.-F., 2002. Modeling wave runup with depth-integrated equations. Coast. Eng. 46, 89–107.

Ma, G., Shi, F., Kirby, J.T., 2012. Shock-capturing non-hydrostatic model for fully dispersive surface wave processes. Ocean Model. 43, 22–35.

Malekmohamadi, I., Bazargan-Lari, M.R., Kerachian, R., Nikoo, M.R., Fallahnia, M., 2011. Evaluating the efficacy of SVMs, BNs, ANNs and ANFIS in wave height prediction. Ocean Eng 38. https://doi.org/10.1016/j.oceaneng.2010.11.020.

Mares-Nasarre, P., Molines, J., Gómez-Mart\'\in, M.E., Medina, J.R., 2021. Explicit Neural Network-derived formula for overtopping flow on mound breakwaters in depth-limited breaking wave conditions. Coast. Eng. 164, 103810.

Mentaschi, L., Besio, G., Cassola, F., Mazzino, A., 2015. Performance evaluation of wavewatch III in the Mediterranean Sea. Ocean Model. 90 https://doi.org/10.1016/j.ocemod.2015.04.003.

Miky, Y., Kaloop, M.R., Elnabwy, M.T., Baik, A., Alshouny, A., 2021. A Recurrent-Cascade-Neural network-nonlinear autoregressive networks with exogenous inputs (NARX) approach for long-term time-series prediction of wave height based on wave characteristics measurements. Ocean Eng 240, 109958.

Oh, J., Suh, K.-D., 2018. Real-time forecasting of wave heights using EOF–wavelet–neural network hybrid model. Ocean Eng 150, 48–59.

Parker, K., Hill, D.F., 2017. Evaluation of bias correction methods for wave modeling output. Ocean Model. 110, 52–65.

Peres, D.J., Iuppa, C., Cavallaro, L., Cancelliere, A., Foti, E., 2015. Significant wave height record extension by neural networks and reanalysis wind data. Ocean Model. 94 https://doi.org/10.1016/j.ocemod.2015.08.002.

Pfister, N., Bauer, S., Peters, J., 2019. Learning stable and predictive structures in kinetic systems. Proc. Natl. Acad. Sci. USA 116, 25405–25411.

Raissi, M., Perdikaris, P., Karniadakis, G.E., 2019. Physics-informed neural networks: a deep learning framework for solving forward and inverse problems involving nonlinear partial differential equations. J. Comput. Phys. 378, 686–707.

Roelvink, D., Reniers, A., Van Dongeren, A.P., De Vries, J.V.T., McCall, R., Lescinski, J., 2009. Modelling storm impacts on beaches, dunes and barrier islands. Coast. Eng. 56, 1133–1152.

Sadeghifar, T., Nouri Motlagh, M., Torabi Azad, M., Mohammad Mahdizadeh, M., 2017. Coastal wave height prediction using recurrent neural networks (RNNs) in the South Caspian Sea. Mar. Geodes. 40 https://doi.org/10.1080/01490419.2017.1359220.

Salatin, R., Chen, Q., Bak, A.S., Shi, F., Brandt, S.R., 2021. Effects of wave coherence on longshore variability of nearshore wave processes. J. Geophys. Res. Ocean. 126, e2021JC017641.

Salim, A., Wilson, G., 2021. Validation and analysis of a 1-D variational assimilation scheme for bathymetry inversion. Coast. Eng. 167, 103895.

Shi, F., Kirby, J.T., Harris, J.C., Geiman, J.D., Grilli, S.T., 2012. A high-order adaptive time-stepping TVD solver for Boussinesq modeling of breaking waves and coastal inundation. Ocean Model. 43, 36–51.

Smit, P.B., Janssen, T.T., Herbers, T.H.C., 2015. Stochastic modeling of inhomogeneous ocean waves. Ocean Model. 96, 26–35.

Sørensen, O.R., Schäffer, H.A., Sørensen, L.S., 2004. Boussinesq-type modelling using an unstructured finite element technique. Coast. Eng. 50, 181–198.

Stringari, C.E., Harris, D.L., Power, H.E., 2019. A novel machine learning algorithm for tracking remotely sensed waves in the surf zone. Coast. Eng. 147, 149–158.

Sun, L., Gao, H., Pan, S., Wang, J.-X., 2020. Surrogate modeling for fluid flows based on physics-constrained deep learning without simulation data. Comput. Methods Appl. Mech. Eng. 361, 112732.

Tolman, H.L., 1991. A third-generation model for wind waves on slowly varying, unsteady, and inhomogeneous depths and currents. J. Phys. Oceanogr. 21 https://doi.org/10.1175/1520-0485(1991)021<0782:atgmfw>2.0.co;2.

Wang, N., Chen, Q., Zhu, L., Sun, H., 2022a. Integration of data-driven and physics-based modeling of wind waves in a shallow estuary. Ocean Model., 101978 https://doi.org/10.1016/j.ocemod.2022.101978.

Wang, N., Chen, Q., Zhu, L., Wang, H., 2022b. Data-driven modeling of wind waves in upper Delaware Bay with living shorelines. Ocean Eng 257, 111669. https://doi.org/10.1016/j.oceaneng.2022.111669.

Wang, S., Teng, Y., Perdikaris, P., 2020. Understanding and Mitigating Gradient Pathologies in Physics-Informed Neural Networks, 04536 arXiv Prepr. arXiv2001.

Wei, Z., 2021. Forecasting wind waves in the US Atlantic Coast using an artificial neural network model: towards an AI-based storm forecast system. Ocean Eng 237, 109646.

Wei, Z., Davison, A., 2022. A convolutional neural network based model to predict nearshore waves and hydrodynamics. Coast. Eng. 171, 104044.

Willard, J., Jia, X., Xu, S., Steinbach, M., Kumar, V., 2020. Integrating Physics-Based Modeling with Machine Learning: A Survey arXiv Prepr. arXiv2003.04919.

Wilson, G., Berezhnoy, S., 2018. Surfzone state estimation, with applications to quadcopter-based remote sensing data. J. Atmos. Ocean. Technol. 35, 1881–1896.

Wilson, G.W., Özkan-Haller, H.T., Holman, R.A., 2010. Data assimilation and bathymetric inversion in a two-dimensional horizontal surf zone model. J. Geophys. Res. Ocean. 115.

Wilson, G.W., Özkan-Haller, H.T., Holman, R.A., Haller, M.C., Honegger, D.A., Chickadel, C.C., 2014. Surf zone bathymetry and circulation predictions via data assimilation of remote sensing observations. J. Geophys. Res. Ocean. 119, 1993–2016.

Zanna, L., Bolton, T., 2020. Data-driven equation discovery of ocean mesoscale closures. Geophys. Res. Lett. 47, e2020GL088376.

Zhang, R., Chen, Z., Chen, S., Zheng, J., Büyüköztürk, O., Sun, H., 2019. Deep long short-term memory networks for nonlinear structural seismic response prediction. Comput. \& Struct. 220, 55–68.

Zheng, Z., Ma, X., Ma, Y., Dong, G., 2020. Wave estimation within a port using a fully nonlinear Boussinesq wave model and artificial neural networks. Ocean Eng 216, 108073.

Zijlema, M., Stelling, G., Smit, P., 2011. SWASH: an operational public domain code for simulating wave fields and rapidly varied flows in coastal waters. Coast. Eng. 58, 992–1012.